



Blunted cone–flare in hypersonic flow

R. Savino *, D. Paterna

*Department of Space Science and Engineering (DISIS), University of Naples “Federico II”,
P. le Tecchio 80, 80125 Napoli, Italy*

Received 25 January 2003; received in revised form 27 July 2003; accepted 3 May 2004

Available online 23 November 2004

Abstract

Computational fluid-dynamics results are presented to show the flowfield around a blunted cone–flare in hypersonic flow. This problem is of particular interest since it features most of the aspects of the hypersonic flow around planetary entry vehicles. The region between the cone and the flare is particularly critical with respect to the evaluation of the surface heat flux. Indeed, flow separation is induced by the shock wave–boundary layer interaction, with subsequent flow reattachment, that can dramatically enhance the surface heat transfer. The exact determination of the extension of the recirculation zone is a particularly delicate task for numerical codes.

Laminar flow computations have been carried out using a full Navier–Stokes solver, with freestream conditions provided by the experimental data obtained in the Von Karman Institute (VKI) H3 Mach 6 wind tunnel.

A grid sensitivity analysis has been performed until grid-solution independence is achieved.

The numerical results are compared with the measured pressure and surface heat flux distributions in the H3 wind tunnel and a good agreement is found, although some discrepancies are present, especially on the length of the recirculation region. A sensitivity analysis has been performed to investigate the influence of the wall temperature, that has shown an influence of the wall temperature on both surface heat flux and surface pressure. A numerical model has been developed to take into account the heating of the test model, and a closer agreement with the experimental data is found.

© 2004 Elsevier Ltd. All rights reserved.

* Corresponding author.

E-mail address: rasavino@unina.it (R. Savino).

1. Introduction

The hypersonic flowfield around a blunted cone–flare exhibits some of the major features of the flows around space vehicles, e.g. a detached bow shock in the stagnation region and the oblique shock wave/boundary layer interaction at the cone–flare junction. The shock wave/boundary layer interaction can produce a region of separated flow. This phenomenon may occur, for example, at the upstream-facing corner formed by a deflected control surface on a hypersonic entry vehicle, where the length of separation has implications for control effectiveness. The phenomenon of shock/boundary-layer interaction has been studied extensively for perfect-gas flows during the past four decades, using experimental and analytical–computational techniques [1–3]. The separation length depends on parameters such as the local Reynolds number $Re_{x_{\text{sep}}}$ and Mach number M_{sep} at separation, the wall-to-edge temperature ratio T_w/T_{sep} , the flare deflection, and the ratio of specific heats [4].

The correct prediction of the separation length poses a challenging task for fluid-dynamics numerical codes. Indeed, apart from the modelling uncertainties associated to turbulence and real-gas effects, there are peculiar simulation difficulties associated to numerical issues such as the spatial accuracy of the numerical code and the computational mesh topology. In order to concentrate only on the numerical aspects of the problem, conditions are chosen so that turbulence and real gas effects are not present. The experimental data considered in the present work are obtained in the H3 hypersonic wind tunnel of the Von Karman Institute (VKI) [5], in laminar conditions and at a freestream Mach number equal to 6, at which real-gas phenomena are negligible and the perfect gas thermodynamic model is acceptable. Two sets of experimental data are available for comparison with numerical results: the surface pressure distribution, obtained by means of electronic pressure transducers, and the surface heat flux, obtained by infrared thermography.

Because of the numerical difficulties associated with the numerical simulation, the cone–flare interaction in a hypersonic flowfield has been selected as test-case in the framework of the FLOWNET test-case database. The FLOWNET network is comprehensive of industries, laboratories and universities and is intended to provide the scientific and industrial communities with a numerical code validation tool and computational/experimental methods in subsonic to hypersonic flow regimes. The FLOWNET test-case database is open to all FLOWNET members and can be accessed online at the web page: www.inria.fr/sinus/flownet.

This paper describes the numerical simulations carried out in the frame of the activities of the FLOWNET network to correlate the experimental results using a finite volume Navier–Stokes solver. In addition, a numerical model has been developed to investigate the effects of the heating of the test model and to explain some discrepancies found between the numerical simulations and the experimental data.

2. Experimental data

The H3 hypersonic wind tunnel of the VKI is composed of an air supply system, where air is heated to temperatures up to 580 K and pressurized up to 32 bar. The gas flows in the axisymmetric nozzle where it expands to a nominal Mach number equal to 6, and enters the test section, where the instrumented test model is located. Finally, air flows through the supersonic diffuser

and it is ejected in the atmosphere. For the present test case, the stagnation pressure is 10 bar and the unit length Reynolds number of the free jet in the test section is $8 \times 10^6 \text{ m}^{-1}$. At this value of the Reynolds number the flow over the entire blunted cone–flare is laminar. The freestream is therefore characterized by the following values of the flowfield parameters [5]:

$$M_\infty = 6$$

$$p_\infty = 673.67 \text{ Pa}$$

$$T_\infty = 67.07 \text{ K}$$

An electronic pressure scanner is used to record the surface pressures during the test, at 25 different surface locations. The test model for the measurement of the pressure is made of aluminium and is shown in Fig. 1.

The spherical nose of the probe has a radius of 3.5 mm, the conical part has an angle of 7.5° with respect to the model axis, while the flare forms an angle of 10° with respect to the cone. The length of the model is 159.11 mm and the cone–flare junction is located at 85.69 mm from the nose [5,6].

The surface temperature is measured by an infrared thermocamera (Agema 900). The plexiglass model of the blunted cone–flare is coated with special paint to increase its emissivity and decrease its reflectivity. The surface heat flux is then obtained using the technique described in [5].

The uncertainties for the pressure and heat transfer measurements are, respectively:

$$\delta\left(\frac{p}{p_\infty}\right) = 7.3\% \quad (1)$$

$$\delta St = 11.5\% \quad (2)$$

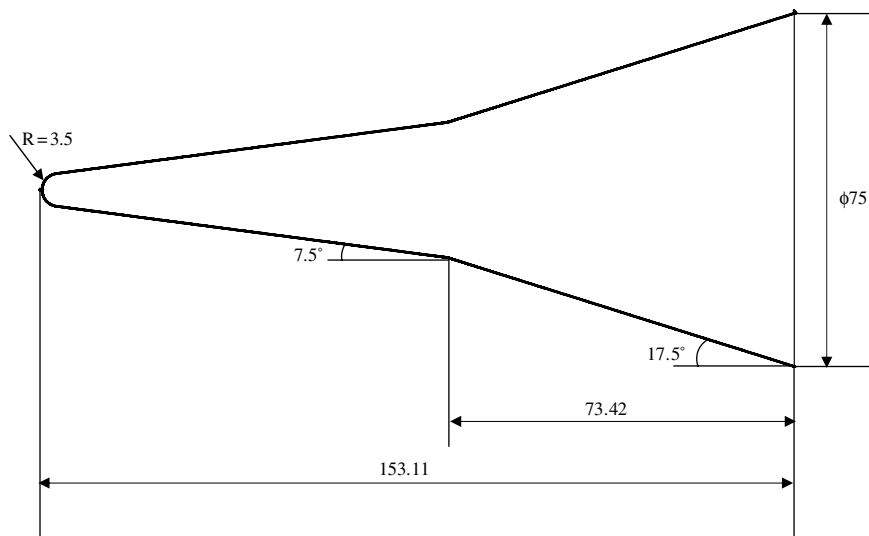


Fig. 1. Geometry of the cone–flare model (linear dimensions in mm).

where p is the wall pressure, St is the Stanton number:

$$St = \frac{\dot{q}}{\rho_{\infty} V_{\infty} c_p (T_w - T_{\infty})} \quad (3)$$

where the subscript w refers to the wall conditions.

Tests repeatability and flow alignment have been checked before providing the experimental data.

3. The model and the numerical code

The air flowing over the cone–flare model has been considered as a perfect gas with the viscosity modelled according to the Sutherland's law:

$$\mu = 1.716 \times 10^{-5} \cdot \left(\frac{T}{273} \right)^{3/2} \frac{384}{T + 111} \text{ kg/(ms)} \quad (4)$$

Thermal conductivity has been derived from the constant Prandtl number assumption ($Pr = 0.74$). The freestream boundary conditions have been imposed on the farfield; no-slip conditions for the velocity, zero normal gradient for pressure and a constant temperature $T_w = 300 \text{ K}$ have been assign on the model wall; symmetry conditions are imposed on the axis.

The system of balance equations (mass, momentum, total energy) with the above mentioned boundary conditions has been solved using the Fluent CFD code, which uses a finite volume method with cell-centered formulation. In particular, the governing equations are discretized on each control volume:

$$\frac{\partial \tilde{\mathbf{U}}}{\partial t} + \frac{1}{V_c} \sum_i (\bar{\mathbf{F}} - \bar{\mathbf{G}})_i \cdot \underline{A}_i = \tilde{\mathbf{S}} \quad (5)$$

where V_c is the control volume and A_i is the generic face enclosing the control volume, and:

$$\tilde{\mathbf{U}} = \frac{1}{V_c} \int_{V_c} \underline{\mathbf{U}} dV_c \quad (6)$$

is the vector of the unknown $(\rho, \rho \underline{V}, \rho E)$ at the cell centres;

$$\bar{\mathbf{F}}_i = \frac{1}{A_i} \int_{A_i} \mathbf{F} dA_i \quad (7)$$

is the vector of the non-dissipative fluxes $(\rho \underline{V}, \rho \underline{V} \underline{V} + p \underline{\underline{U}}, \rho \underline{V} H)$ at the face centres;

$$\bar{\mathbf{G}}_i = \frac{1}{A_i} \int_{A_i} \mathbf{G} dA_i \quad (8)$$

is the vector of the dissipative fluxes $(0, \underline{\tau}, \underline{\tau} \cdot \underline{V} + \underline{\dot{q}})$, with $\underline{\underline{U}}$ the unit tensor, $\underline{\tau}$ the stress tensor and $\underline{\dot{q}}$ the heat flux vector.

Non-dissipative fluxes on each boundary face A_i are computed according to the semidiscrete self-adjusting hybrid method proposed by Jameson et al. [7]. Considering only the inviscid fluxes

in Eq. (5), and no source terms, the first-order version of this upwind method is based on the following positions:

$$\frac{\partial \tilde{U}}{\partial t} = -\frac{1}{V_c} \sum_i \bar{\mathbf{F}}_i \cdot \underline{A}_i \quad (9)$$

with

$$\bar{\mathbf{F}}_i = \theta_i \bar{\mathbf{F}}_i^{(1)} + \max \left(0, 1 - \frac{\theta_i}{\delta} \right) \bar{\mathbf{F}}_i^{(2)} \quad (10)$$

where

$$\bar{\mathbf{F}}_i^{(1)} = \frac{1}{2} (\bar{\mathbf{F}}_{i,R} + \bar{\mathbf{F}}_{i,L}) - \frac{1}{2} \rho(A_m) (\underline{U}_R - \underline{U}_L) \quad (11)$$

$$\bar{\mathbf{F}}_i^{(2)} = \frac{1}{2} (\bar{\mathbf{F}}_{i,R} + \bar{\mathbf{F}}_{i,L}) + \frac{1}{2} \delta \rho(A_m) \underline{H}(\underline{U}) \quad (12)$$

where θ_i is a shock switch, ρ is the spectral radius (i.e. the largest eigenvalue) of the flux jacobian $\frac{\partial \mathbf{F}}{\partial \underline{U}}$ and A_m is the flux jacobian evaluated in correspondence of the *Roe average* states [8]; δ is a user-adjustable parameter, and $\underline{H}(\underline{U})$ is a function of the unknowns evaluated in correspondence of the current computational cell and its neighbours [9]. The subscripts R and L denote conditions evaluated at the right and left, respectively, of the face A_i .

The right and left states are computed from a multidimensional linear reconstruction approach to obtain a second order upwind scheme [10].

Dissipative fluxes are computed by the Gauss' theorem.

Time integration is performed by an explicit 5-stage Runge-Kutta scheme. The time step is constrained by the CFL (Courant–Friedrichs–Lewy) condition. Using the Swanson–Tukel shock switch [11] and an appropriate choice for the parameter δ , the largest permissible CFL number is 1.5. Each grid cell is computed at the same CFL number, so that convergence toward steady state is accelerated (local time stepping).

4. Results at constant wall temperature

The base computational grid is shown in Fig. 2. It is composed of 9600 quadrilateral cells, with 240 cells in the direction tangential to the body and 40 cells in the normal direction.

The normal spacing of the first cell is 3×10^{-6} m in the stagnation region (nose), 1×10^{-5} m in the cone–flare junction region. The values of the normal spacing have been chosen to ensure that the surface heat fluxes are accurately predicted.

The spacing distribution along the stagnation line, Δn , is shown in Fig. 3. Here y is the normal coordinate to the body starting from the stagnation point. Fig. 4 shows the tangential spacing Δs (along the body), with x the axial coordinate originating from the stagnation point.

The mesh is clustered in the cone–flare junction to better capture the interaction between the boundary layer and the oblique shock wave on the flare. Two finer meshes are obtained by

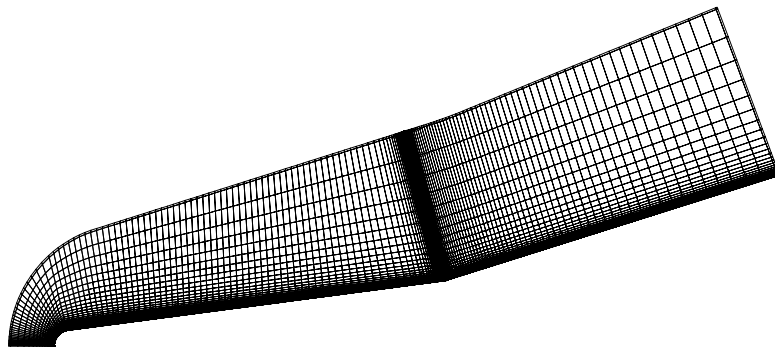


Fig. 2. Coarsest computational mesh (240×40 cells).

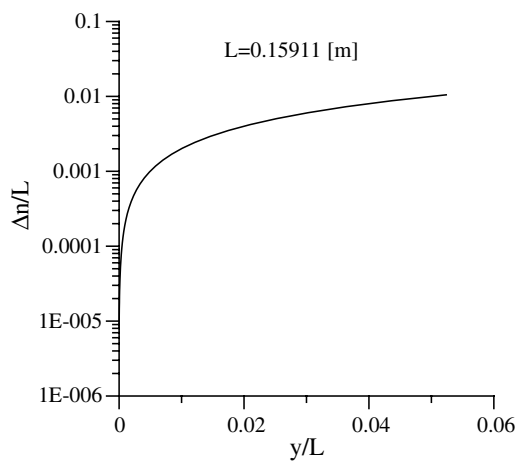


Fig. 3. Mesh spacing along the stagnation line (240×40 cells).

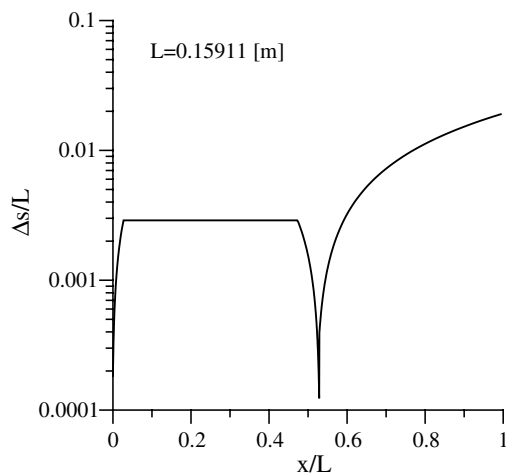


Fig. 4. Mesh spacing along the body (240×40 cells).

Table 1
Grid spacing values

Grid	Δn_0	Δn_h	Δs_0	Δs_h
240×40	$3e-6$	$1e-5$	$6.75e-5$	$1.8e-5$
480×80	$1.5e-6$	$5e-6$	$3.37e-5$	$9e-6$
960×160	$0.75e-6$	$2.5e-6$	$1.68e-5$	$4.5e-6$

0 = stagnation point; h = cone–flare junction.

successively subdividing the basic one in equal parts. Table 1 summarizes the characteristics of the mesh utilized for the computations.

Fig. 5 shows the Mach number contours in the flowfield, corresponding to the finest mesh solution. The most relevant features of the flow can be detected: the detached bow shock wave around the nose and the characteristic shock wave–boundary layer interaction in the cone–flare junction region.

Fig. 6 shows a zoomed view of the stagnation region, in terms of pressure and temperature. The stagnation pressure value of 31,482 Pa and post-shock temperature value of 549 K are in good agreement with the normal shock theory (which provides 31,538 Pa and 533 K, respectively). The computed value of the stagnation-point heat flux is about 226 kW/m^2 , for all meshes. Therefore, the solution is grid converged, as for the stagnation region, and yields a value of the stagnation-point heat flux in excellent agreement with the Fay–Riddell formula (221.8 kW/m^2) [12]. In Fig. 7 the computed shock shape is compared with the results obtained by the semi-empirical Bilig formula [13]. The bow shock wave is progressively weakened as it departs from the stagnation region. The curvature of the shock wave produces an entropy layer where vorticity is present and where the variation of the flow variables with the distance from the body cannot be neglected, even out of the boundary layer (Fig. 8).

The shock wave/boundary layer interaction in the cone–flare junction determines a flow separation, as shown by the velocity vectors pattern of Fig. 9. The separation shock and the reattachment shock intersect forming a corner shock (as shown by the computed pressure isolines in Fig. 10) that gives rise to a shear layer parallel to the flare surface.

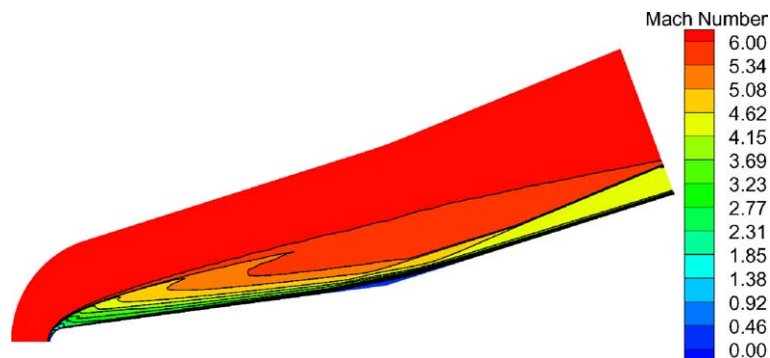


Fig. 5. Mach number contours.

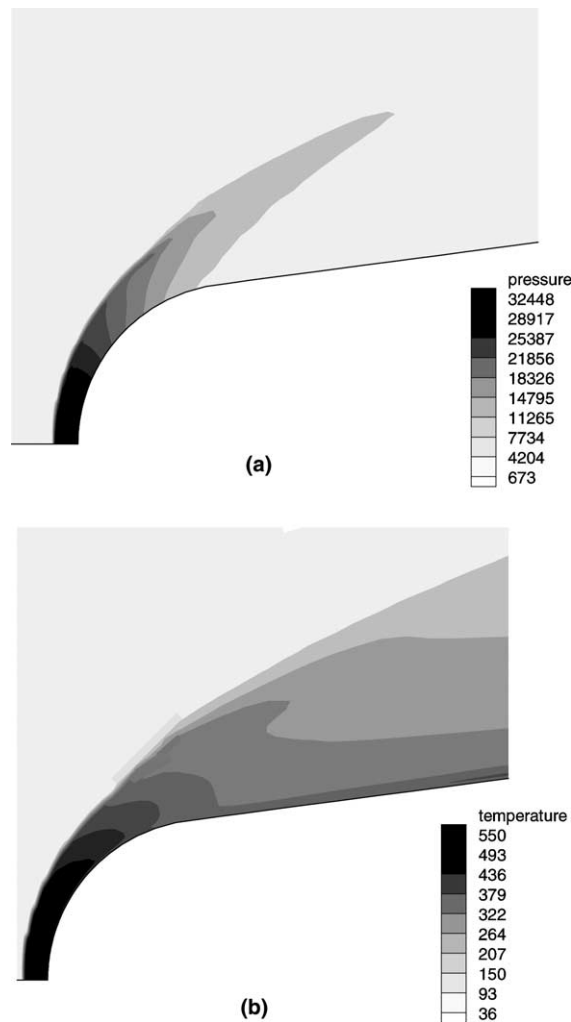


Fig. 6. Pressure (a) and temperature (b) contours in the stagnation region.

The shear layer is shown in Fig. 10 by the colored contours of the velocity magnitude, that are superimposed to the pressure isolines. The scale in Fig. 10 has been enlarged in the radial direction to better show the shock wave interactions.

This is the most critical area of the flowfield, since the extension of the laminar separation bubble is very much grid dependent. In the separation zone, a first shock occurs that determines the separation of the flow and a rise in pressure, see Fig. 11.

Then, a region of recirculating flow follows, determining a characteristic “plateau” in the pressure distribution, Fig. 11.

After the cone–flare junction, a second shock determines the reattachment of the flow, with consequent rise in both pressure and surface heating. The dimension of the separated area can be obtained by the profile of the skin friction coefficient, Fig. 12.

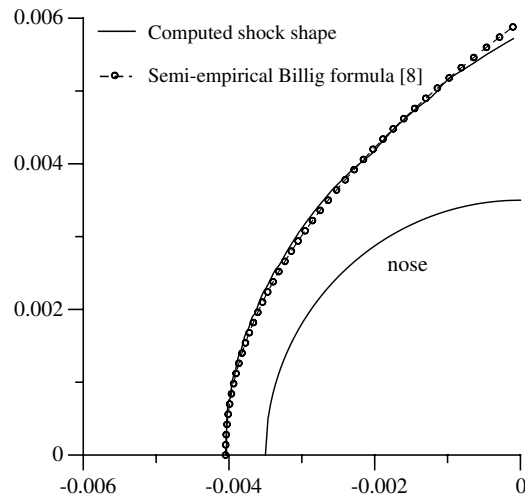


Fig. 7. Comparison of the computed shock shape with the one derived from Billig formula [13].

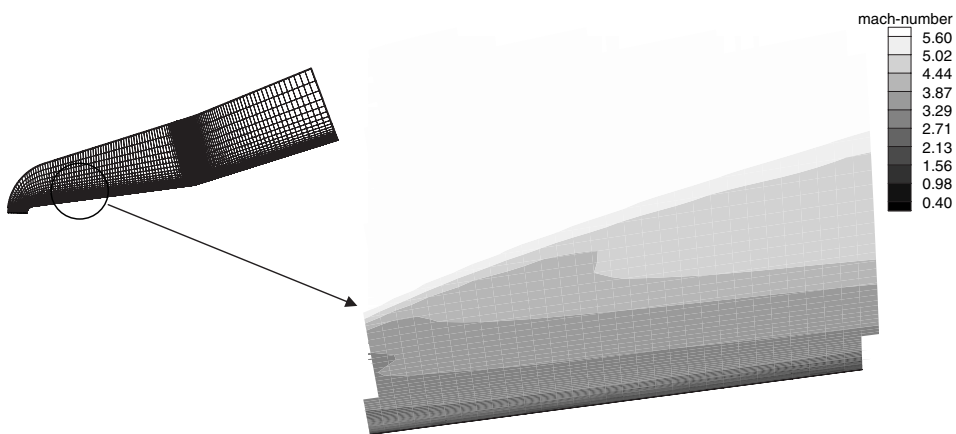


Fig. 8. Mach number contours in the entropy layer.

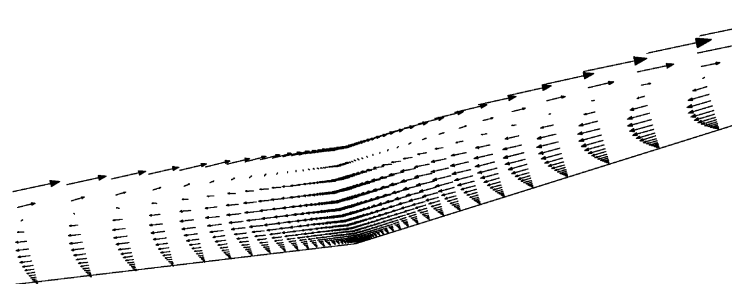


Fig. 9. Zoomed view of the recirculation zone.

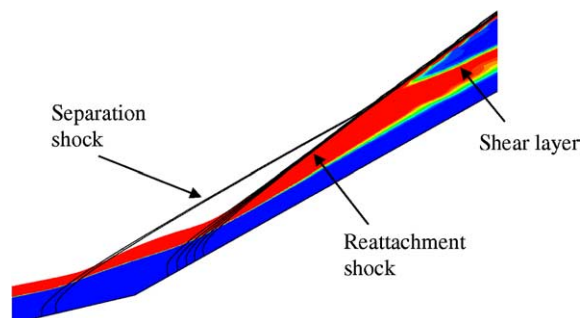


Fig. 10. Shock wave–boundary layer interaction at the cone–flare junction. Pressure isolines and velocity magnitude contours.

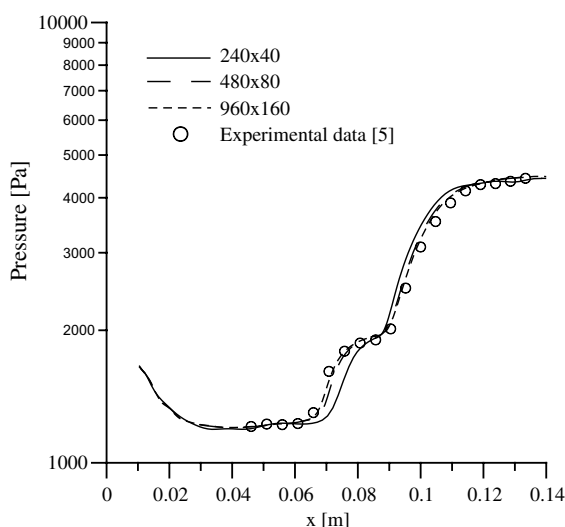


Fig. 11. Influence of mesh size on wall pressures.

The skin friction profiles corresponding to the three different meshes used are plotted in Fig. 12 for comparison. It can be noted that the extension of the separation bubble increases with the mesh refinement. The coarsest mesh is not able to capture the recirculation zone dimension, giving a separation point located at $x = 76.5$ mm and a length of separation $L_{\text{sep}} = 19.79$ mm, while the finest mesh provides a separation point at $x = 72.73$ mm and a separation length $L_{\text{sep}} = 26.43$, much closer to the experimental findings (Table 2). The same considerations hold for the surface profiles of the pressure (Fig. 11) and heat flux (Fig. 13), where the characteristic V-shape distribution can be observed.

Figs. 11 and 13 also show the comparison between computed and experimental results.

Ahead of the separation zone, the numerical computations overestimate the experimental results, both for the pressure and for the heat flux. This behaviour has been related in [5] to the flow non-uniformity in the test section. In the reattachment zone, the results obtained on the coarsest

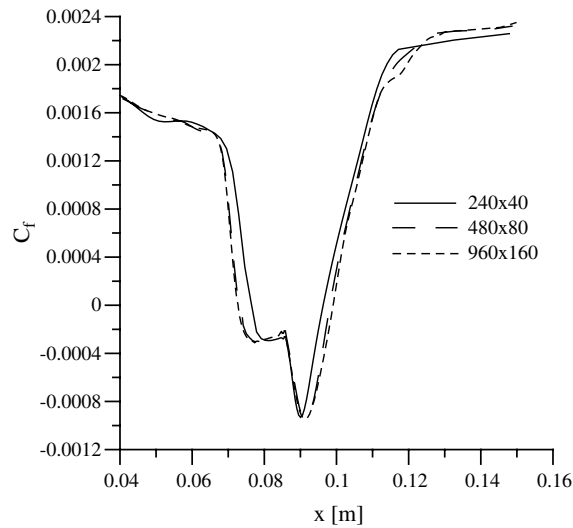


Fig. 12. Skin friction coefficient in the separation zone.

Table 2

Separation and reattachment locations

	Grid 480 × 80	Grid 960 × 160	$\Delta\%$
q_0 (W/m ²)	226,687	226,332	−0.15
q_h (W/m ²)	15,400	15,197	−1.33
x_{sep} (mm)	76.5	72.73	−1.06
x_{rea} (mm)	96.23	99.16	0.84

0 = stagnation point; h = cone–flare junction; sep = separation; rea = reattachment.

mesh overestimate the peak heating, while the finest mesh solution is in much better agreement with the experimental data.

5. Effects of the wall temperature

As discussed in [5], the measurements are carried out after a certain delay of time (about 3 s in the case of pressure measurements), and therefore the temperature of the model is certainly higher than its initial value, due to the relatively high heat fluxes at the hypersonic conditions.

To evaluate the sensitivity of the results to the wall temperature, a simulation has been carried out assuming a wall temperature 10% higher ($T_w = 330$ K) than in the previous simulations. The results, in terms of surface heat flux and surface pressure are shown in Figs. 14 and 15, respectively.

Fig. 14 shows that, as expected, the surface heat flux is lower than in the previous case ($T_w = 300$ K) and that the peak heat flux after flow reattachment ($x \cong 0.11$ m) decreases in a non-negligible way (about 15%).

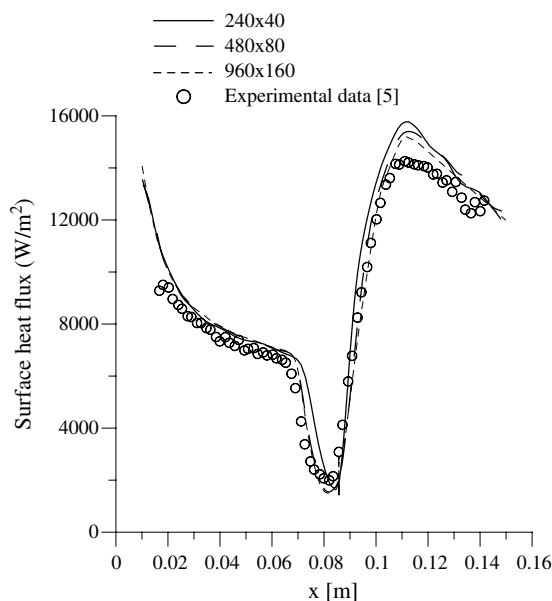


Fig. 13. Influence of mesh size on wall heat fluxes.

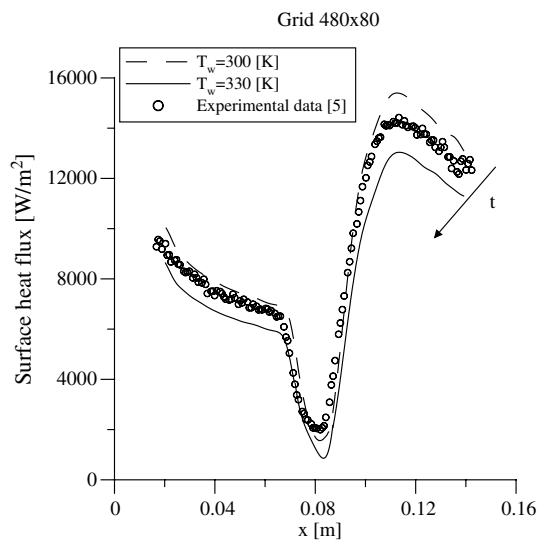


Fig. 14. Effect of the wall temperature on surface heat flux.

Fig. 15 shows that also the wall pressure is affected by the surface temperature, and, in particular, the length of the separation bubble seems to increase with temperature, approaching more closely the experimental results.

These results have motivated a further investigation of the effects of the wall temperature, taking into account the effective heating of the test model during the experiment.

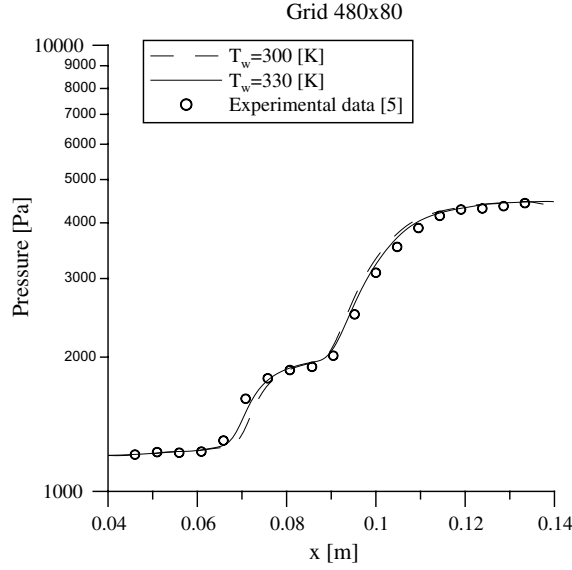


Fig. 15. Effect of the wall temperature on surface pressure.

A numerical model has been developed that allows the simultaneous solution of the fluid-dynamic equations and the energy equation in the solid model:

$$\frac{\partial T}{\partial t} = \alpha \nabla^2 T \quad (13)$$

where α is the solid thermal diffusivity.

The unsteady Navier–Stokes equations and the energy equation in the solid are solved by a second-order fully implicit scheme. The coupling between the two solutions is provided by the global radiative equilibrium condition:

$$\dot{q}_c = \dot{q}_r + \dot{q}_s \quad (14)$$

assuming that the convective heat flux at the model surface (\dot{q}_c) is equal, at each point, to the radiative heat flux leaving the surface (\dot{q}_r) plus the heat flux in the solid model (\dot{q}_s).

By substituting in (14) the expression of each heat flux, we obtain:

$$\lambda \frac{\partial T}{\partial n} \Big|_c = \varepsilon \sigma (T^4 - T_a^4) + \lambda_s \frac{\partial T}{\partial n} \Big|_s \quad (15)$$

where T is the temperature, λ the thermal conductivity of air, λ_s the thermal conductivity of the solid, ε its surface emissivity, n the local surface normal, and σ the Stefan–Boltzmann constant. The subscript ‘a’ refers to ambient conditions.

Condition (15) cannot be directly implemented in the Fluent code. Therefore an “ad hoc” user-defined function (udf) has been developed. Derivatives appearing in Eq. (15) have been discretized using a first-order approximation. The resulting equation reads:

$$\varepsilon \sigma T_w^4 + \left(\frac{\lambda_s}{\Delta_s} + \frac{\lambda}{\Delta_c} \right) T_w - \left(\frac{\lambda_s T_s}{\Delta_s} + \frac{\lambda T_c}{\Delta_c} + \varepsilon \sigma T_a^4 \right) = 0 \quad (16)$$

where T_w is the local wall temperature, Δ_c and Δ_s the distance of the first cell centre from the wall, in the air and solid computational domain, respectively.

This fourth-order algebraic equation has been solved for T_w , at each step of the global iterative algorithm, by a Newton–Raphson method.

According to Dieudonné [5], the test model for the measurement of the wall pressure was made of aluminium, while the model for the measurement of the surface heat flux was made of plexiglass, with the nose in aluminium to withstand the high temperatures in the stagnation region. Therefore, two unsteady numerical simulations have been carried out, with a plexiglass model and an aluminium model, considering as initial conditions (time $t = 0$) the fluid-dynamic field obtained in the previous simulation with the intermediate grid (480×80). The geometry of the model and the corresponding mesh are shown in Fig. 16. The grid-point distribution on the model surface has a one-to-one correspondence with the surface grid in the fluid phase (conformal grids). The properties of the simulated materials are reported in Table 3.

The results of the simulation with the plexiglass model are shown in Figs. 17 and 18. Fig. 17 shows the transient wall temperatures in the separation region. The wall temperatures quickly change with time. The peak surface temperature after flow reattachment rises up to 345 K after 3 s. The corresponding heat flux profiles are shown in Fig. 18. The heat flux distribution, as already noted above, is particularly sensitive to the wall temperature distribution. In particular, after only 0.1 s, the heat flux profile matches more closely the experimental data. This can be seen both in the region ahead of the cone–flare junction, and in the reattachment zone. The length of the separation region increases with time, and, at $t = 0.1$ s, is 2.97 cm, against the initial length of 2.53 cm.

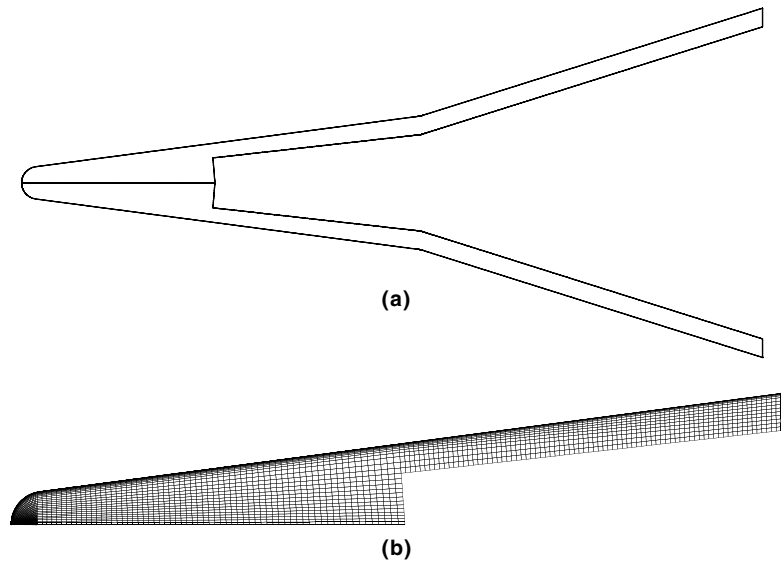


Fig. 16. (a) Geometry of the test model and (b) particular of the mesh in the nose region.

Table 3

Properties of models materials

Material	Thermal conductivity ($\text{W m}^{-1} \text{K}^{-1}$)	Thermal diffusivity ($\text{m}^2 \text{s}^{-1}$)	Surface emissivity
Plexiglass	0.18	8.55×10^{-5}	1
Aluminium	202.4	1.08×10^{-7}	1

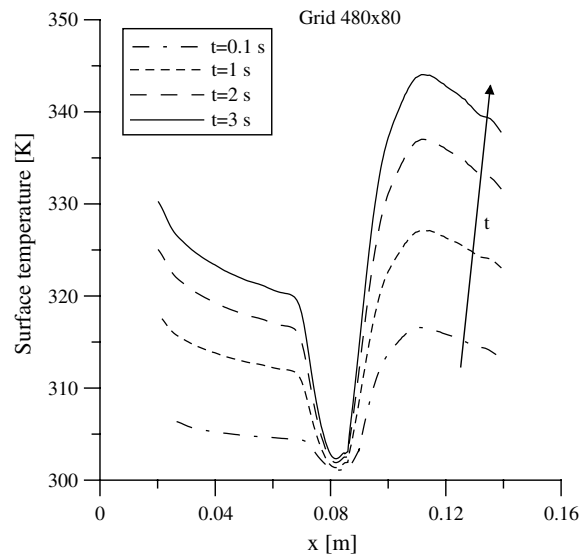


Fig. 17. Wall temperature profiles along the surface of the plexiglass model.

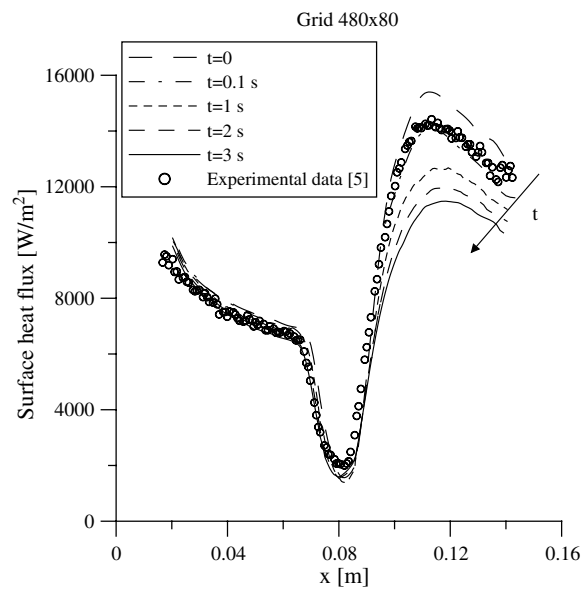


Fig. 18. Heat flux profiles along the surface of the plexiglass model.

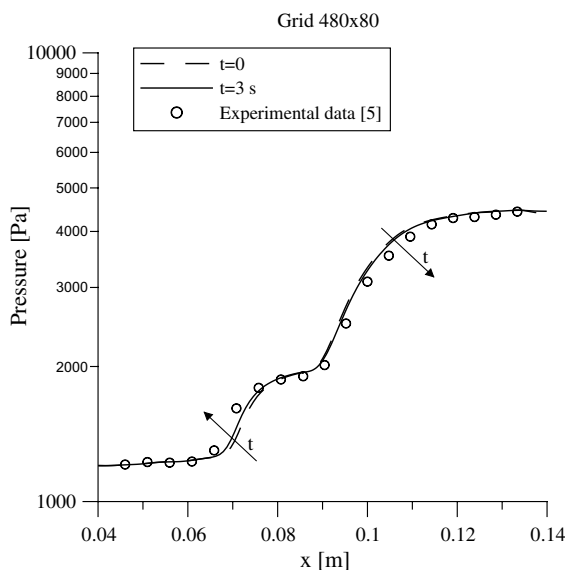


Fig. 19. Wall pressure distribution on the aluminium model.

The wall pressure distribution has been computed with the aluminium model, and is shown in Fig. 19. According to [5], the time response of the pressure acquisition system requires a 3 s delay between the model insertion and the pressure data recording. Therefore, the pressure profile after 3 s is reported in the graph of Fig. 19, and seems to be in better agreement with the experimental data. In particular, the length of the recirculation region is in this case $L_{\text{sep}} = 2.69$ cm at $t = 3$ s. The choice of a finer grid could further improve the comparison between numerical and experimental results.

6. Conclusions

A computational fluid-dynamic analysis of the hypersonic flow around a blunted cone–flare has been performed. The freestream conditions correspond to the exit nozzle conditions of the H3 wind tunnel at the Von Karman Institute (VKI). The conditions are chosen so that the flow over the cone–flare remains laminar for the entire length of the model. Numerical computations are performed on different grid levels to study the solution sensitivity to the mesh spacing. The grid sensitivity analysis has shown negligible differences between the intermediate and the finest grids, both on the surface heat fluxes and the wall pressures in the recirculation. The results show that the main features of the flow are correctly predicted, and the results are in fair agreement both with numerical computations from literature and with the available experimental data.

The role of the surface temperature has been pointed out, showing that the heat flux and the wall pressure distribution are sensitive to small temperature differences. In particular, taking into account the heating of the test model, the numerical model seems to better reproduce the experimental results.

References

- [1] Anders JB. Wedge-induced laminar-boundary-layer separation on a flat plate in low-density, hypervelocity flow, NASA TN D-5791, 1970.
- [2] Hayakawa K, Squire LC. The effect of the upstream boundary-layer state on the shock interaction at a compression corner. *J Fluid Mech* 1982;122(6):369.
- [3] Fay JF, Sambamurthi J. Laminar hypersonic flow over a compression corner using the HANA code, AIAA Paper 92-2896, 1992.
- [4] Katzer E. On the lengthscales of laminar shock/boundary-layer interaction. *J Fluid Mech* 1989;206:477.
- [5] Dieudonne W, Boerrigter HL, Charbonnier JM. Hypersonic flow on a blunted cone-flare in the VKI-H3 Mach 6 wind tunnel, Technical Note TN-193, Von Karman Institute, 1999.
- [6] Dieudonne W. Hypersonic flow over axisymmetric bodies, Von Karman Institute Project Report 1995-18, 1994.
- [7] Jameson A, Schmidt W, Turkel E. Numerical solution of the Euler equations by finite volume methods using Runge-Kutta time-stepping schemes. Technical Report AIAA-81-1259, AIAA 14th Fluid and Plasma Dynamics Conference, Palo Alto, California, June 1981.
- [8] Roe PL. Characteristic based schemes for the Euler equations. *Ann Rev Fluid Mech* 1986;18:337–65.
- [9] Laney CB. Computational gas dynamics. Cambridge University Press; 1998.
- [10] Barth TJ, Jespersen D. The design and application of upwind schemes on unstructured meshes. Technical Report AIAA-89-0366, AIAA 27th Aerospace Sciences Meeting, Reno, Nevada, 1989.
- [11] Swanson RC, Turkel E. On central-difference and upwind schemes. *J Comput Phys* 1992;101:292–306.
- [12] Hankey WL. Re-entry aerodynamics, AIAA Education Series, 1988.
- [13] Billig FS. Shock-wave shapes around spherical- and cylindrical-nosed bodies. *J Spacecraft Rockets* 1967;4(6): 822–823.